Measurement 218 (2023) 113139

Contents lists available at ScienceDirect

Measurement

journal homepage: www.elsevier.com/locate/measurement

Structural optimization and dynamic calibration for load sharing dynamic force measurement platform based on MIGA and SVR

Chengbo Zhou [a,b], Mingyi Xia [a,*], Chenghao Li [a,b], Zhenbang Xu [a,b,*]

[a] Changchun Institute of Optics, Fine Mechanics and Physics, Chinese Academy of Science, Jilin Changchun 130033, China
[b] Center of Materials Science and Optoelectronics Engineering, University of Chinese Academy of Sciences, Beijing 100049, China

ARTICLE INFO

Keywords:
Vibration
Measuring platform
Dynamic force
Load sharing
MIGA
SVR

ABSTRACT

In order to quantify dynamic forces/moments on the ground, a high-performance platform is necessary. This article improves the performance of the measurement platform from both structure and calibration. The platform's loading capacity and base frequency have been significantly increased by the introduction of an innovative load sharing ring, which also allows the platform to have other important and practical characteristics. Further improvements in platform performance are then achieved by optimizing the platform parameters using a multi-island genetic algorithm (MIGA). In addition, the calibration method is improved. The maximum relative error and cross-coupling error for the novel non-linear support-vector-regression-based (SVR) method are 3.42% and 6.54%, respectively, which are much superior than the 9.98% and 15.39% for the traditional linear least-squares-based (LS) calibration method, indicating better accuracy and decoupling performance of the SVR-based dynamic calibration. This has important implications for measuring dynamic forces and improving the stability of equipment in spacecraft.

1. Introduction

The demands on the performance of the China Space Station Telescope (CSST) continue to increase as the requirements for research in space continue to grow. For instance, stellar radial velocities with an accuracy of 2–4 km s^{-1} can be provided by the CSST for AFGKM-type stars [1], aiming at high spatial resolution targets imaging of approximately 0.15″ covering a huge area of the vision about 17,500 deg^2 and a wide wavelength range from NUV to NIR [2]. Small dynamic disturbance forces can then have a significant effect on the performance of the telescope; thus, there is a need for an accurate ground-based measurement device for measuring the dynamic disturbance forces of vibration sources from the telescope. Additionally, vibrating components on spacecraft are becoming heavier and larger [3]. With other mounting equipment, the measuring devices are typically required to hold loads in excess of 1 ton in a test [4], and each functional module has a diameter of over 1 m. In summary, a dynamic force measurement platform with a larger mounting surface, higher load capacity, high fundamental frequency, and good measuring accuracy is required.

There are a number of previous studies that improve the performance of measurement devices structurally [5–13]. For instance, traditional devices based on the Stewart platform [5–7] are loosely structured, making it difficult to guarantee high stiffness and good fundamental frequency under heavy loads, and they are costly to manufacture and install. Li [8] therefore used a four-point support structure for the sensor design, which is simple and offers good properties in terms of heavy loading measurements and base frequency. However, as the mounting surface and load increase, the fundamental frequency of the four-point support structure decreases significantly. Xia [3] then proposed an eight-point-support platform that is capable of measuring dynamic forces/moments from huge sources, but its measurement principle leads to redundant measurement, which inevitably introduces systematic errors. After that, Li [9–11] designed a four-point supported force sensor with a load sharing ring that has good decoupling performance and can provide excellent load capacity with a high fundamental frequency. Once the basic structure was determined, the structural parameters would be optimized to further improve the performance of the measurement device. Take Sun [14] and Han [15] for example, they used response surface methodology (RSM) and design of experiments (DOE) to obtain optimal sensor parameters, allowing the stiffness and sensitivity of the sensors to be optimized. Despite the fact that DOE makes the computational complexity of optimization much lower, it makes the

* Corresponding authors at: Changchun Institute of Optics, Fine Mechanics and Physics, Chinese Academy of Science, Jilin Changchun 130033, China (Z. Xu).
E-mail addresses: xiamingyi@ciomp.ac.cn (M. Xia), xuzhenbang@ciomp.ac.cn (Z. Xu).

https://doi.org/10.1016/j.measurement.2023.113139
Received 25 November 2022; Received in revised form 24 May 2023; Accepted 30 May 2023
Available online 7 June 2023

optimization results inaccurate. Structural optimization based on multi-objective optimization algorithms [16–18] gives relatively better optimization results, with which the multi-island genetic algorithm (MIGA) is widely used due to its global optimization capability and good robustness.

Furthermore, the performance of the measuring device, mainly in terms of measurement accuracy, can be improved by modifying the measurement method. Liu [19] and Li [8,11], for example, derived theoretical models of measurement after the structural design of the measuring device, but many of the theoretical models are based on assumptions, making the derivation difficult and error-prone. Xia [3], Sun [14], Liu [20], etc. used the least squares (LS) based calibration method, which offers acceptable measurement performance. Nonetheless, the LS algorithm neglects the nonlinear part of the device by treating it as a linear system and suffers from matrix singularity, which makes the calibration applications limited and prone to errors. On the other hand, calibrations based on intelligent algorithms are gradually being applied. By way of example, Liang [21] and Wang [22] used the neural networks (NN) algorithm for static calibration of sensors; Oh [23] adopted deep learning (DL) for calibration; and least squares support vector machine regression (LSSVR) was employed by Li [24] for calibration. These intelligent algorithm based calibrations are good at resolving the nonlinear terms that appear in the system and perform better in terms of accuracy and coupling errors. However, previous research has been limited to static calibration. On the one hand, static calibration can not eliminate the influence of the fundamental frequency of the large equipment itself on the measurement accuracy, and on the other hand, research on intelligent algorithms for static calibration cannot be directly applied to dynamic calibration.

Above all, this paper illustrates a load sharing measurement platform and improves the performance of the platform through structural optimization and the dynamic calibration method. The paper is organized as follows: Section 2 presents the structural design of the measurement platform, optimizes its structural parameters through MIGA, and compares the optimization results of MIGA and ASA. Measurements based on LS and support vector regression (SVR) dynamic calibration approaches are investigated in Section 3, and the processes of both calibration methods are described in detail. The results are discussed in Section 4. The work of this paper is summarized in Section 5.

2. Structural design and optimization

2.1. Structure design

A load sharing measurement platform consisting of a load platform, a load sharing ring, a base, and four sensors is shown in Fig. 1. The load platform's mounting surface is designed to be 500 × 500 mm, which is larger than the majority of measuring platforms on the market. If the load platform and the base are connected by sensors only, the rigidity, fundamental frequency, and the platform's load capacity can not be guaranteed, and the subsequent dynamic calibration is meaningless. Thereby, in addition to the four squarely distributed sensors, a load sharing ring is also installed, which is placed in parallel with the sensors. The ring increases the platform's loading capacity and the base frequency. Both the ring and the sensors are bolted to the base and the load platform.

The structure of the sensor is shown in Fig. 2, consisting of an installation shell, a rigid insulation layer, and force sensing elements. Wherein, threaded holes in the installation shell are used for connection between the load platform and base. Force sensing elements are composed of crystals with compression or shear effects, enabling each sensor to output forces in the X, Y, and Z directions. The sensors are preloaded during manufacture using preload equipment.

In order to increase the load sharing capacity of the ring, the material is selected as 40Cr [10]. The material properties of the measuring platform are shown in Table 1, where the properties of the sensors were obtained experimentally. There will undoubtedly be some inaccuracies in the ensuing optimization and simulation due to the approximation of the experiments.

2.2. Structure optimization

The suitable platform parameters can significantly increase the load capacity and fundamental frequency, in addition to reducing manufacturing costs and assembly requirements. Therefore, the structural parameters of the platform need to be optimized.

The objective of optimization is to find the seven optimal structural parameters in red lettering shown in Fig. 1 to maximize the fundamental frequency Fq, minimize the maximum stress $\sigma_{\max}$ under a Z-direction force of 1000 N (characterizing the load capacity) and the sum of the area of the bottom surface of the sensors and the ring S (characterizing the manufacturing cost and assembly difficulty). Based on design and machining experience, the optimization weight of S is set to 0.5 and the weight of the remaining objective functions to 1. The optimization problem can therefore be formulated as equation (1) and Table 2.

$$\begin{gathered}\text{Maximize } Fq \ (\text{weight} = 1),\\ \text{Minimize } \sigma_{\max} \ (\text{weight} = 1),\ S \ (\text{weight} = 0.5),\\ \text{Design variable } b,\ H,\ hr,\ hs,\ R,\ rr,\ rs,\\ \text{Subject to } 3\leqslant b\leqslant 30 \text{ mm},\ 15\leqslant H\leqslant 60 \text{ mm},\ 15\leqslant hr\leqslant 60 \text{ mm},\ 15\leqslant hs\leqslant 60 \text{ mm},\\ 150\leqslant R\leqslant 290 \text{ mm},\ 5\leqslant rr\leqslant 40 \text{ mm},\ 5\leqslant rs\leqslant 30 \text{ mm},\ Fq\geqslant 1000 \text{ Hz}\end{gathered} \tag{1}$$

where seven design variables are the wall thickness of the load sharing ring b, the height of the load platform H, the height of the load sharing ring h_r, the height of the sensor h_s, the radius of the sensor distribution R, the radius of the load sharing ring r_r, and the radius of the sensor r_s.

There are a number of measures to solve the optimization problem, of which the multi-island genetic algorithm (MIGA) is an enriched and easy-to-execute one based on the traditional genetic algorithm (GA). As a pseudo-parallel algorithm, MIGA has superior global solving capability and faster convergence than GA. The MIGA is a more suitable way to solve problems where gradient information is difficult to obtain and is now widely used in structural design. The MIGA has several islands, and

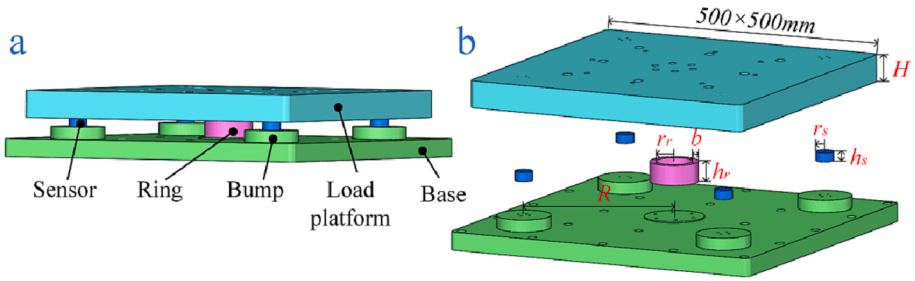

Fig. 1. The model of the load sharing measuring platform: (a) front view; (b) exploded view.

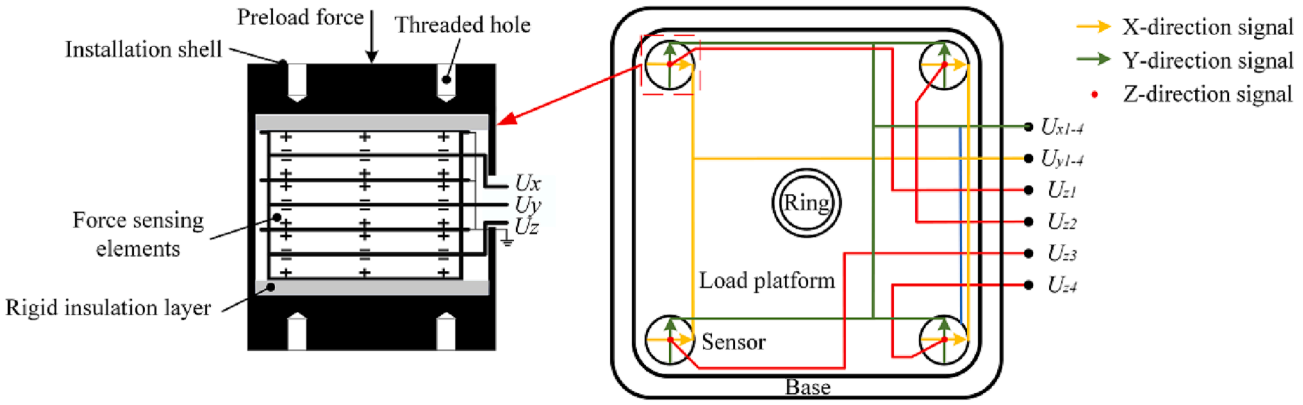

Fig. 2. Schematic diagram of the load sharing measurement platform.

each island has individuals (sub-populations). It is assumed that individuals can migrate between each island, and the ones with the ability to migrate are the superior ones (elites) that have better genes and perform genetic operations on the new islands, helping the algorithm to jump beyond local to global optimum.

The process of optimizing the platform structure based on MIGA is shown in Fig. 3. (1) Generate the initial population $\mathbf{P}_0$ and encode the individuals. (2) Disperse the $\mathbf{P}_0$ on several islands. (3) Use scripts to alter the geometric model, modify the finite element model, and perform simulations to evaluate the fitness of the individuals. (4) When the migration conditions are met, the elites migrate between the different islands. (5) Perform the genetic process on each island, including selection, crossover, and mutation. (6) If the termination condition is satisfied, stop the search and obtain the optimal solution. (7) Repeat steps 3 to 6.

According to Fig. 3, the MIGA code is programmed and embedded with three execution scripts. In this study, the number and size of the islands are set to 10, the number of generations is 20 (i.e., $a = m = 10$, maxgen = 20), and the crossover rate, mutation rate, and migration rate are 1.00, 0.01, and 0.01, respectively. The objective function and penalty during the 2000 iterations and 20 generations of the platform optimization using MIGA are shown in Figs. 4 and 5, respectively (Fig. 5 displays the best solution in each generation). It can be concluded that the optimal solution has been found at the 15th migration. The optimal structural parameters and objective function values based on MIGA are shown in Table 3. The measuring platform has a 1st order frequency of 1020.2 Hz and a maximum stress of 3.8 MPa under a Z-direction force of 1000 N.

In addition, a structural optimization code based on the adaptive simulated annealing (ASA) algorithm is written for testing. As shown in Fig. 6, the optimal solution is found after it is iterated 333 times, with the optimal structural parameters and objective function values shown in Table 4. The platform optimized by ASA has a slightly higher fundamental frequency than that obtained by MIGA, but has a lower load capacity, significantly higher manufacturing costs and installation requirements. It can be inferred that the optimal solution of MIGA is superior to that of ASA, and ASA's optimal solution may be local rather than global.

To further illustrate the superiority of the design structure of the platform, the optimal structural parameters obtained by MIGA are also used to model a platform without the ring. As shown in Fig. 7, the model is then meshed and subjected to finite element analysis to obtain a 1st order frequency of 719.9 Hz and a maximum stress of 6.4 MPa under a Z-direction force of 1000 N. Consequently, the base frequency and loading capacity of the measuring platform with a load sharing ring increase by 41.7% and 68.4%, respectively, compared to the platform without a ring. From the above analysis, it can be concluded that the performance of the platform in terms of fundamental frequency and load capacity is significantly improved by optimizing the structure of the measuring platform with the load sharing ring.

In addition, the designed platform has other excellent and unexpected properties. Finite element simulations of the measurement platforms with and without the load sharing ring are carried out, and different mass sources are installed on both platforms. The fundamental frequency curves for the two platforms are obtained as depicted in Fig. 8. According to the diagram, the fundamental frequencies are not the same when each platform is fitted with sources of different masses, which means that the transfer functions of each platform are not the same when different sources are installed onto the platform. It is then necessary to re-calibrate the platform dynamically before each measurement of a different source to improve the accuracy of the measurement. It is worth noting that when the source mass is not large (<20 kg), as shown in the green box in Fig. 8, the mass has no essential effect on the 1st frequency of the platform with the ring, which facilitates the measurement of small mass sources.

Table 1
Platform structural material properties.

Component	E (MPa)	ν	ρ (kg/m^3)
Load platform & Base	2.06×10^5	0.3	7.85×10^3
Load sharing ring	2.06×10^5	0.3	7.85×10^3
Sensors	7.65×10^4	0.32	7.5×10^3

3. Dynamic calibration

3.1. Traditional calibration method based on LS

The dynamic calibration equipment, shown in Fig. 9a, consists of a load sharing platform, a calibration tool (self-made; the force sensors

Table 2
Structural parameters' optimization range and objective function.

Range of variables							Target of the objective function		
b (mm)	H (mm)	h_r (mm)	h_s (mm)	R (mm)	r_r (mm)	r_s (mm)	Σ_{max} (MPa)	Fq (Hz)	S (mm^2)
3 ~ 30	15 ~ 60	15 ~ 60	15 ~ 60	150 ~ 290	5 ~ 40	5 ~ 30	min	Max & >1000	min

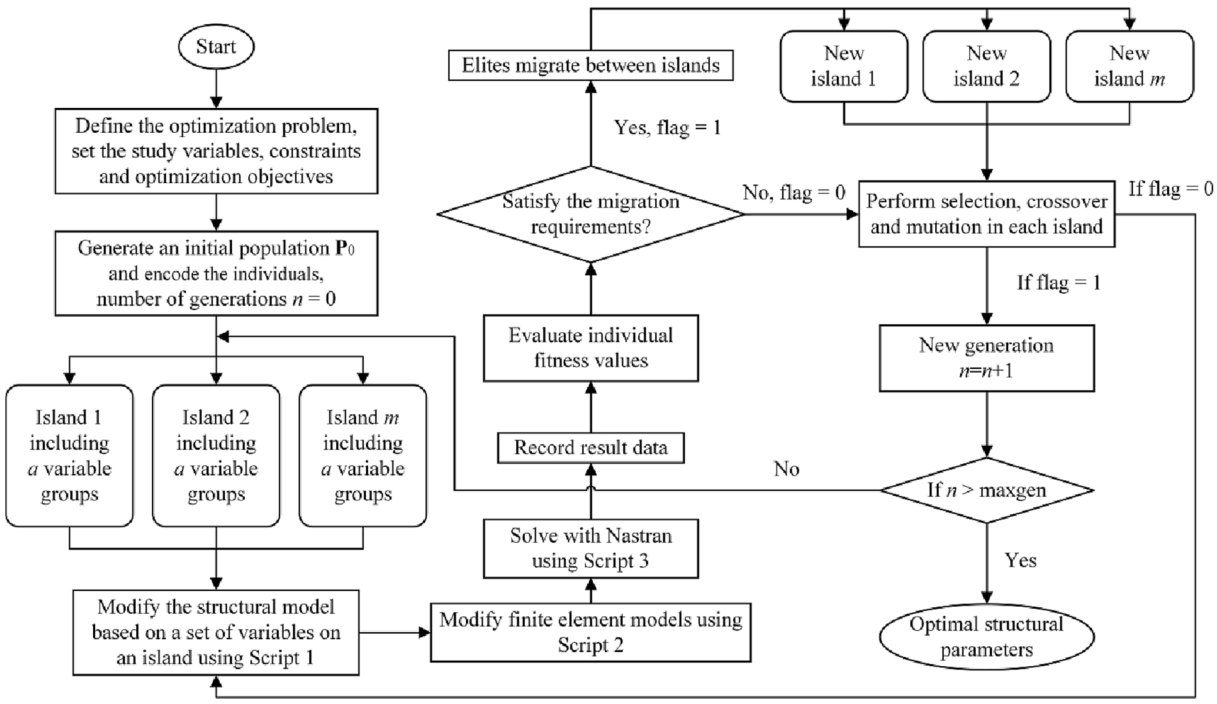

Fig. 3. Structure optimization process based on MIGA.

used in the tool are 208C02, PCB), a portable measuring arm (8725–6, Hexagon Absolute Arm 6-Axis [27], not displayed), a vibration source [25] (shown in Fig. 9c, relative error: < 3.33%), a charge amplifier (YE5853, Sinocera), a digital data acquisition (652u-24 bit, IOtech), and a PC. The calibration tool is used to input impulsive forces to the source horizontally or vertically [28], the vibration source is employed to generate the desired dynamic disturbance forces, and the output signals from sensors can be collected by the digital data acquisition in real time.

Before the calibration, three impulsive forces with different amplitudes were input at the same point of the platform using the calibration tool, and the three responses of one sensor were recorded. Then the transfer functions between the input point and output sensor can be obtained, as indicated in Fig. 10. It is shown in the figure that the measurement platform's fundamental frequency is 1096 Hz, which is in general accordance with the results of the simulation (1020.2 Hz), thanks to the simplicity of the model.

The platform was then conventionally calibrated. In this study, six forces were input using the calibration tool, and the six-dimensional forces/moments in space should be covered. Assume the six input forces are as follows:

$$\boldsymbol{F}_{\text{input}}(\omega) = [\boldsymbol{F}_1(\omega)\ \boldsymbol{F}_2(\omega)\ \boldsymbol{F}_3(\omega)\ \boldsymbol{F}_4(\omega)\ \boldsymbol{F}_5(\omega)\ \boldsymbol{F}_6(\omega)]^{\mathrm{T}} \tag{2}$$

where $\mathbf{F}_i(\omega)$ is one of the six input forces. Then $\mathbf{F}_{\text{input}}(\omega)$ can be converted to $\mathbf{F}_o(\omega)$ with reference to the center O of the measuring platform by the conversion matrix $\mathbf{C}_{6\times6}$ [26], which is measured by the portable measuring arm [27]:

$$\boldsymbol{F}_o(\omega) = \boldsymbol{C}\boldsymbol{F}_{\text{input}}(\omega) \tag{3}$$

Besides, six outputs are expressed as:

$$\boldsymbol{U}\mathrm{c}(\omega) = [\boldsymbol{U}_{\mathrm{c}1}(\omega)\ \boldsymbol{U}_{\mathrm{c}2}(\omega)\ \boldsymbol{U}_{\mathrm{c}3}(\omega)\ \boldsymbol{U}_{\mathrm{c}4}(\omega)\ \boldsymbol{U}_{\mathrm{c}5}(\omega)\ \boldsymbol{U}_{\mathrm{c}6}(\omega)]^{\mathrm{T}} \tag{4}$$

where $\mathbf{U}_{ci}(\omega)$ is the 1×6 voltage output vector from four sensors as shown in Fig. 2, and the subscript c implies calibration. The dynamic calibration matrix between the platform inputs and outputs can then be obtained as follows:

$$\boldsymbol{G}(\omega) = \boldsymbol{F}_o(\omega)\boldsymbol{U}_c(\omega)^{\mathrm{T}}[\boldsymbol{U}_c(\omega)\boldsymbol{U}_c(\omega)^{\mathrm{T}}]^{-1} = \boldsymbol{C}\boldsymbol{F}_{\text{input}}(\omega)\boldsymbol{U}_c(\omega)^{\mathrm{T}}[\boldsymbol{U}_c(\omega)\boldsymbol{U}_c(\omega)^{\mathrm{T}}]^{-1} \tag{5}$$

In this case, the dynamic disturbance forces/moments can be

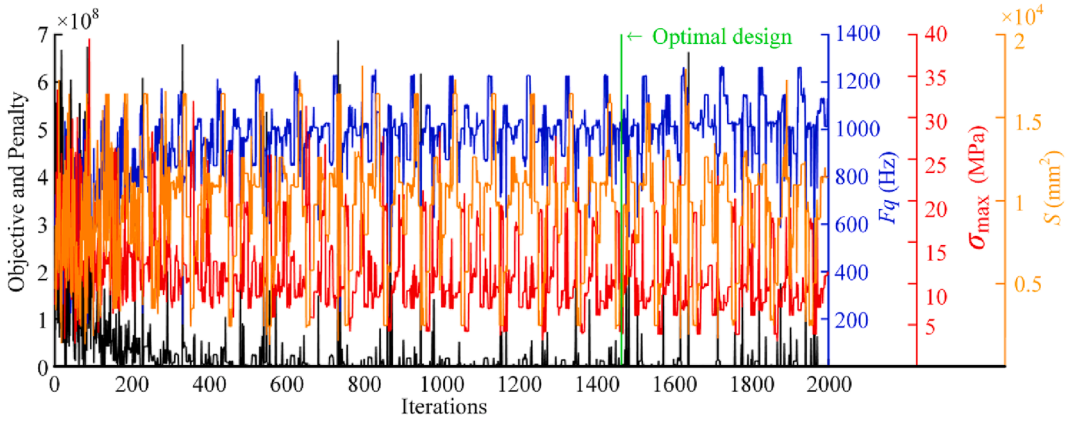

Fig. 4. 2000 iterations of the MIGA optimization process.

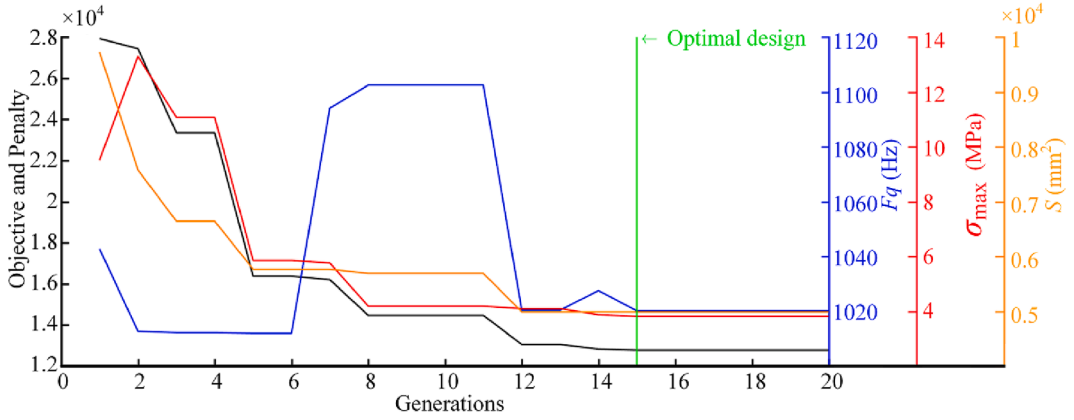

Fig. 5. 20 generations of the MIGA optimization process.

Table 3
Structural optimum parameters and objective functions based on MIGA.

Optimum parameters							Corresponding objective function		
b (mm)	H (mm)	h_r (mm)	h_s (mm)	R (mm)	r_r (mm)	r_s (mm)	Σ_{max} (MPa)	Fq (Hz)	S (mm^2)
12	51	33	15	254	32	13	3.819	1020.2	4988.8

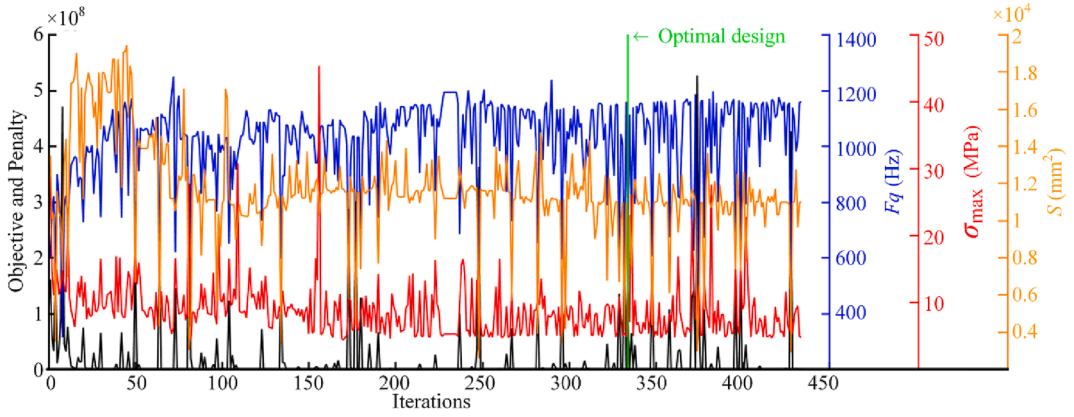

Fig. 6. ASA optimization process.

Table 4
Structural optimum parameters and objective functions based on ASA.

Optimum parameters							Corresponding objective function		
b (mm)	H (mm)	h_r (mm)	h_s (mm)	R (mm)	r_r (mm)	r_s (mm)	Σ_{max} (MPa)	Fq (Hz)	S (mm^2)
10	54	55	32	243	13	28	4.810	1157.6	10983.0

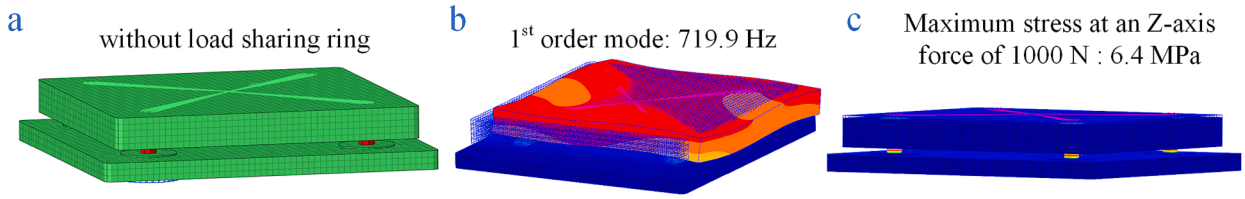

Fig. 7. FEA for the platform without the load sharing ring: (a) meshed model; (b) the first order mode of the platform; (c) stress cloud diagram for the platform subjected to Z-direction force.

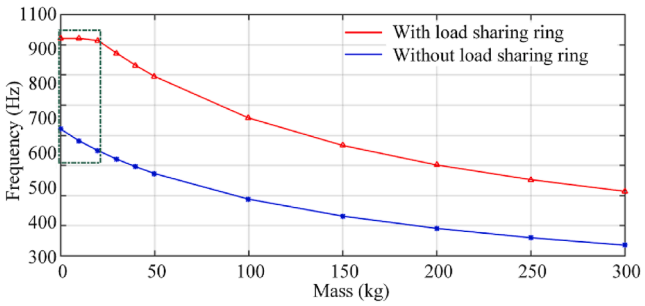

Fig. 8. Fundamental frequencies of two platforms with different mass sources.

measured using the calibration matrix **G**(ω):

$$\boldsymbol{F}(\omega) = \boldsymbol{G}(\omega)\ \boldsymbol{U}(\omega) \tag{6}$$

where **F**(ω) is the vector of measured forces/moments, and **U**(ω) refers to the vector of actual output voltages.

After that, the measurements of the z-axis impulsive force and y-axis impulsive moment generated by the vibration source (simulator [25]) were carried out based on the dynamic calibration method described above. The measurement was taken at a sampling frequency of 2048 Hz and a sampling time of 16 s, and the results are shown in Fig. 11. The reason for choosing impulsive forces as input is to verify the performance of the platform over the full frequency bandwidth of 1/16 to 800 Hz. In addition, the same measurements were performed for the remaining forces/moments in four directions. The statistics for the average relative error rates and cross-coupling error rates are shown in Table 5, where the data in bold on the diagonal are relative error rates. The maximum relative error rate and cross-coupling error rate are 9.98% and 15.39%, respectively. Importantly, the average relative error rates and cross-coupling error rates for the forces/moments in each dimension are calculated according to equations (7) and (8). Where $E_{r\text{-}m}$ denotes the relative error of the force/moment in the m^{th} dimension, $E_{c\text{-}mn}$ denotes the cross-coupling error rate of the n^{th} dimensional force/moment on the m^{th} dimensional force/moment, $F_{\text{in-}m}(\omega_a)$ denotes the input force/moment in the m^{th} dimension at a frequency of ω_a, and $F_{\text{out-}m}(\omega_a)$ denotes the output force/moment in the m^{th} dimension at a frequency of ω_a.

$$Er-m = \frac{1}{12800}\sum_{a=1}^{12800}\frac{|Fin-m(\omega a)-Fout-m(\omega a)|}{Fin-m(\omega a)}\times 100\%(m = 1,2,\cdots,6) \tag{7}$$

$$Ec-mn = \frac{1}{12800}\sum_{a=1}^{12800}\frac{Fout-n(\omega a)}{Fin-m(\omega a)}\times 100\%(m = 1,2,\cdots,6; n = 1,2,\cdots,6;\ n \neq m) \tag{8}$$

However, there are a variety of problems with the above least squares (LS) approach for measurement. Firstly, it considers the

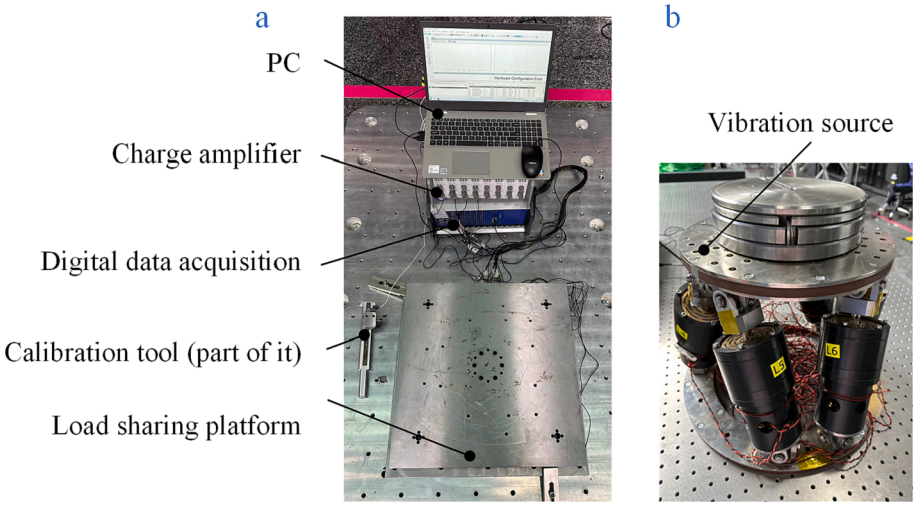

Fig. 9. Dynamic calibration equipment for the platform.

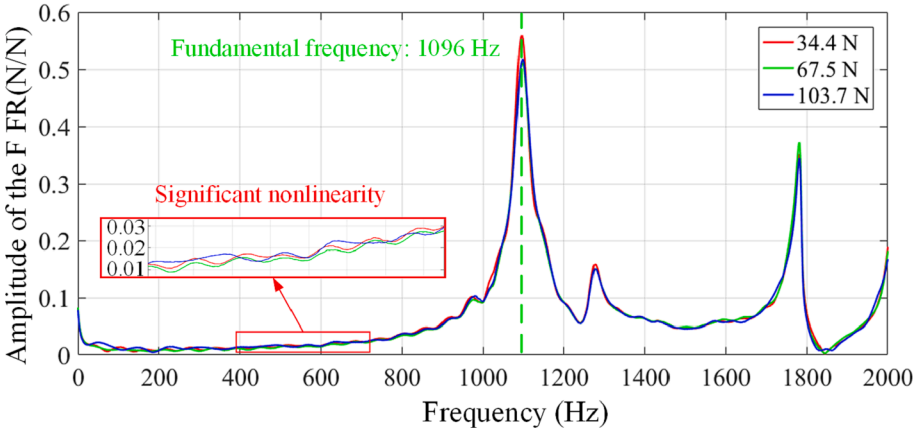

Fig. 10. Transfer functions of the measurement platform.

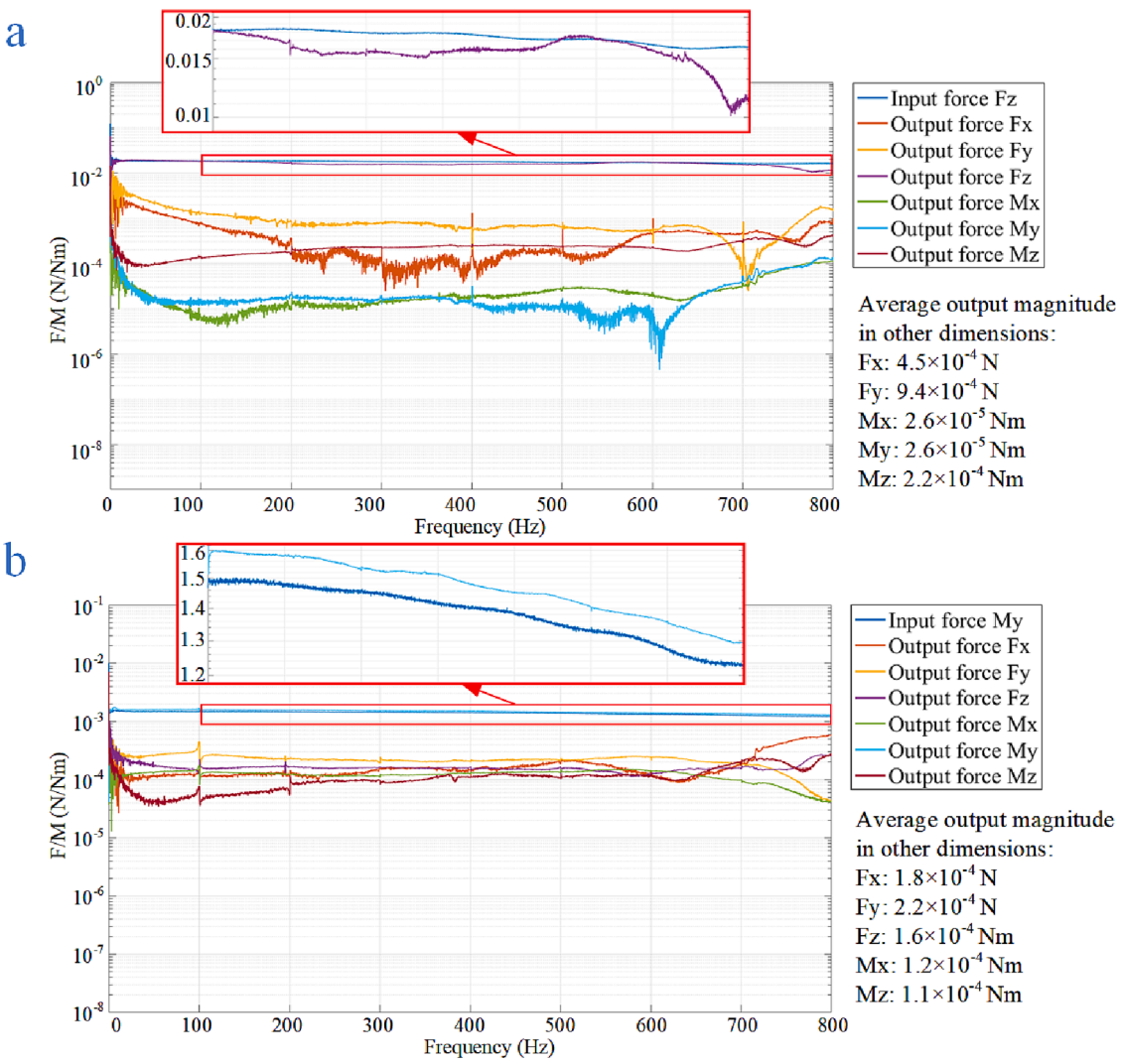

Fig. 11. Comparison of input and output forces based on LS: (a) F_z; (b) M_y.

Table 5
Average relative error rates and cross-coupling error rates for the platform based on the LS.

Forces/Moments (N/Nm)	**Average relative error rates** & cross-coupling error rates					
	F_x	F_y	F_z	M_x	M_y	M_z
F_x	**6.894**	0.869	2.537	9.578	13.01	12.78
F_y	1.563	**8.165**	5.256	11.72	15.39	9.956
F_z	3.975	1.167	**8.586**	10.57	11.67	10.14
M_x	5.357	4.372	0.153	**7.669**	8.607	8.871
M_y	0.389	3.751	0.152	8.98	**6.323**	9.743
M_z	4.407	1.534	1.286	7.172	8.209	**9.982**

platform as a linear system, ignoring the nonlinear characteristics of the platform. Nevertheless, it is clear from Fig. 10 that the dynamic linearity of the platform is not ideal due to the increased mounting surface and mass of the measurement platform. Additionally, $\mathbf{U}_c(\omega)$ in Eq. (5) is susceptible to the problem of singular matrices, which affects the accuracy of the measurement. Thus, there is a need for an alternative dynamic calibration method that can overcome these drawbacks.

3.2. Improved calibration method based on SVR

The load sharing dynamic measurement platform is a multi-input and multi-output nonlinear system. Therefore, the approach of support vector regression (SVR) is introduced to solve the cross-coupling problem of the nonlinear system.

The support vector machine (SVM) nonlinear decoupling model is illustrated in Fig. 12. The sequence of the input and output $(x_i(\omega), y_i(\omega))$ can be regarded as a set, where $x_i(\omega)$ is the collected output signal and $y_i(\omega)$ is the input force. Then, the set of training samples can be represented as:

$$\mathrm{T}(\omega) = \backslash\{\ (x1(\omega), y1(\omega)), (x2(\omega), y2(\omega)), \cdots, (xk(\omega), yk(\omega))\backslash\}\ ,\ xi(\omega) \in \mathrm{R}^6, yi(\omega) \in \mathrm{R}^6, i = 1, 2, \cdots, k \tag{9}$$

Transformation functions are then used to transform the training samples into a high-dimensional vector space:

$$\phi(x(\omega)) = (\varphi(x1(\omega)), \varphi(x2(\omega)), \cdots, \varphi(xk(\omega))) \tag{10}$$

After that, the linear problem in the higher dimension, converted from the non-linearity problem in the lower dimension, can be expressed as equation (11):

$$f(x(\omega)) = w(\omega)\phi(x(\omega)) + b(\omega) \tag{11}$$

where $w(\omega)$ is the weight in the higher dimensional space and $b(\omega)$ is the deviation. If $w(\omega)$ and $b(\omega)$ can be derived, then Eq. (11) can be applied to measure.

The SVR problem can then be formalized as:

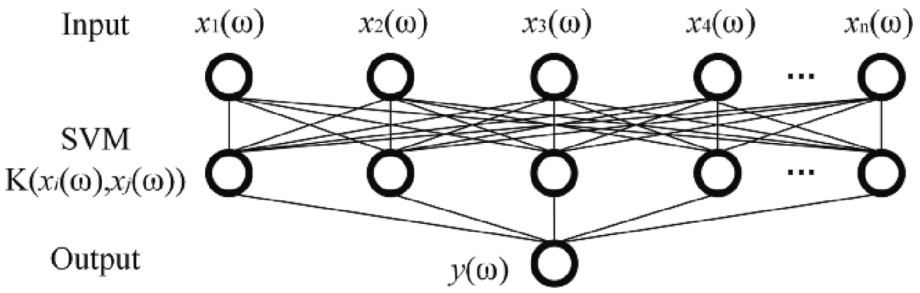

Fig. 12. Structure diagram of the nonlinear decoupling model by SVM.

$$\min_{w(\omega),b(\omega)} \frac{||w(\omega)||^2}{2} + C(\omega)\sum_{i=1}^{n}\varepsilon i(\omega) \tag{12}$$

where $C(\omega)$ is the regularization constant and $\varepsilon_i(\omega)$ is penalized using an insensitive loss function. The introduction of the slack variables allows equation (12) to be rewritten as:

$$\begin{aligned}\min_{w(\omega),b(\omega),\xi i(\omega),\xi^* i(\omega)} \frac{||w(\omega)||^2}{2} + C(\omega)\sum_{i=1}^{n}(\xi i(\omega) + \xi^* i(\omega))\\ \text{s.t. } f(xi(\omega)) - yi(\omega) \leqslant \varepsilon i(\omega) + \xi i(\omega),\\ yi(\omega) - f(xi(\omega)) \leqslant \varepsilon i(\omega) + \xi^* i(\omega),\\ \xi i(\omega) \geqslant 0, \xi^* i(\omega) \geqslant 0, i = 1, 2, \cdots, n\end{aligned} \tag{13}$$

By introducing the Lagrangian operators $\alpha(\omega)$, $\alpha^*(\omega)$, $\beta(\omega)$, $\beta^*(\omega)$, the optimization problem can be transformed into a pairwise problem. Since $\varepsilon(\omega)$ and $C(\omega)$ are artificially given parameters, and $\zeta(\omega)$,$\zeta^*(\omega)$, $\beta(\omega)$, $\beta^*(\omega)$ can be offset in the calculation, the pairwise problem can be expressed, after reorganizing and using the Gauss radial basis kernel, as:

By solving equation (14) and considering the mapping relationship, $w(\omega)$ and $b(\omega)$ in Eq. (11) can be derived. Then, Equation (11) can be used for dynamic force measurements.

The input forces shown in Eq. (15) are used as output samples of SVR training, and the output voltages shown in Eq. (16) are used as input samples of SVR training. Such samples $\{\mathbf{F}(\omega), \mathbf{U}(\omega)\}$ have 120 sets at each frequency, i.e., $n = 120$ (forces of different magnitudes are input 20 times at each of the 6 input points). The SVR model can be obtained after training.

$$\boldsymbol{F}(\omega) = [Fx(\omega)Fy(\omega)Fz(\omega)My(\omega)My(\omega)Mz(\omega)]^{\mathrm{T}} \tag{15}$$

$$\boldsymbol{U}(\omega) = [U1(\omega)U2(\omega)U3(\omega)U4(\omega)U5(\omega)U6(\omega)]^{\mathrm{T}} \tag{16}$$

The flow of the SVR dynamic calibration is presented in Fig. 13, where the trained SVR models for each frequency are obtained. The *fft* is the number of sampling points, which equals 12800.

Based on the above, the six impulsive forces/moments in the previous subsection (no re-input or re-capture required) were re-measured using the model obtained by SVR. Set SVR's maximum number of

$$\begin{aligned}J = -\frac{1}{2}\sum_i\sum_j[\alpha i(\omega) - \alpha^* i(\omega)][\alpha j(\omega) - \alpha^* j(\omega)]K(xi(\omega)xj(\omega)) - \sum_i[\alpha i(\omega) + \alpha^* i(\omega)]\varepsilon(\omega) + \sum_i[\alpha i(\omega) - \alpha^* i(\omega)]f(xi(\omega))\\ \text{s.t. } 0 \leqslant \alpha i(\omega), \alpha^* i(\omega) \leqslant C\end{aligned} \tag{14}$$

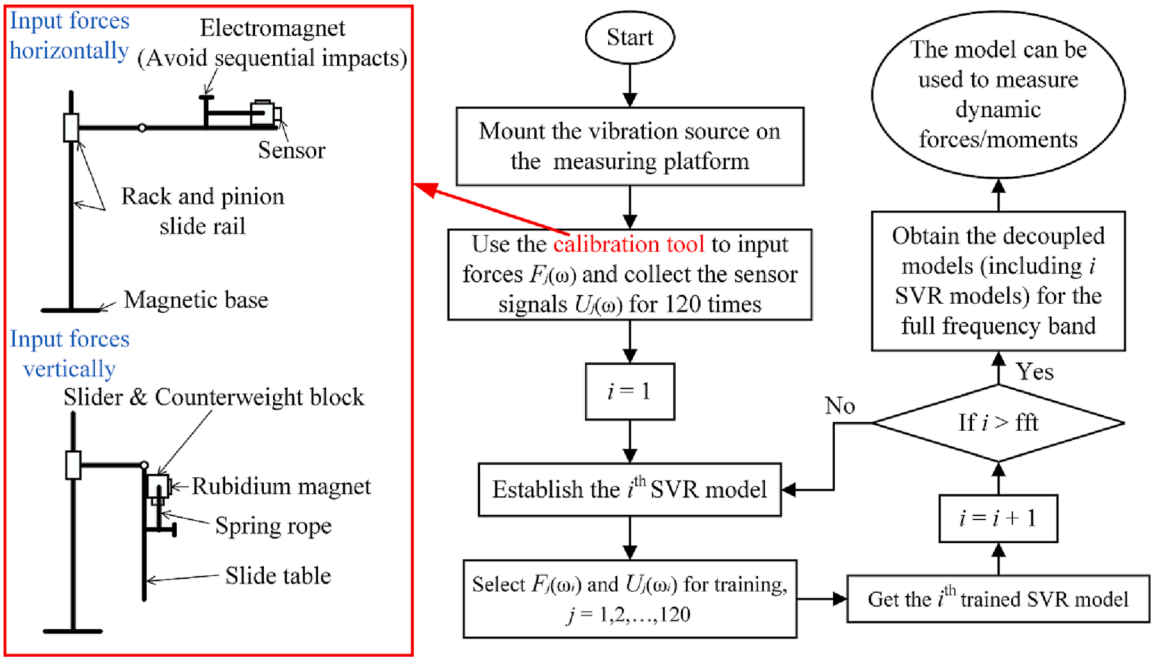

Fig. 13. Process for dynamic calibration based on SVR.

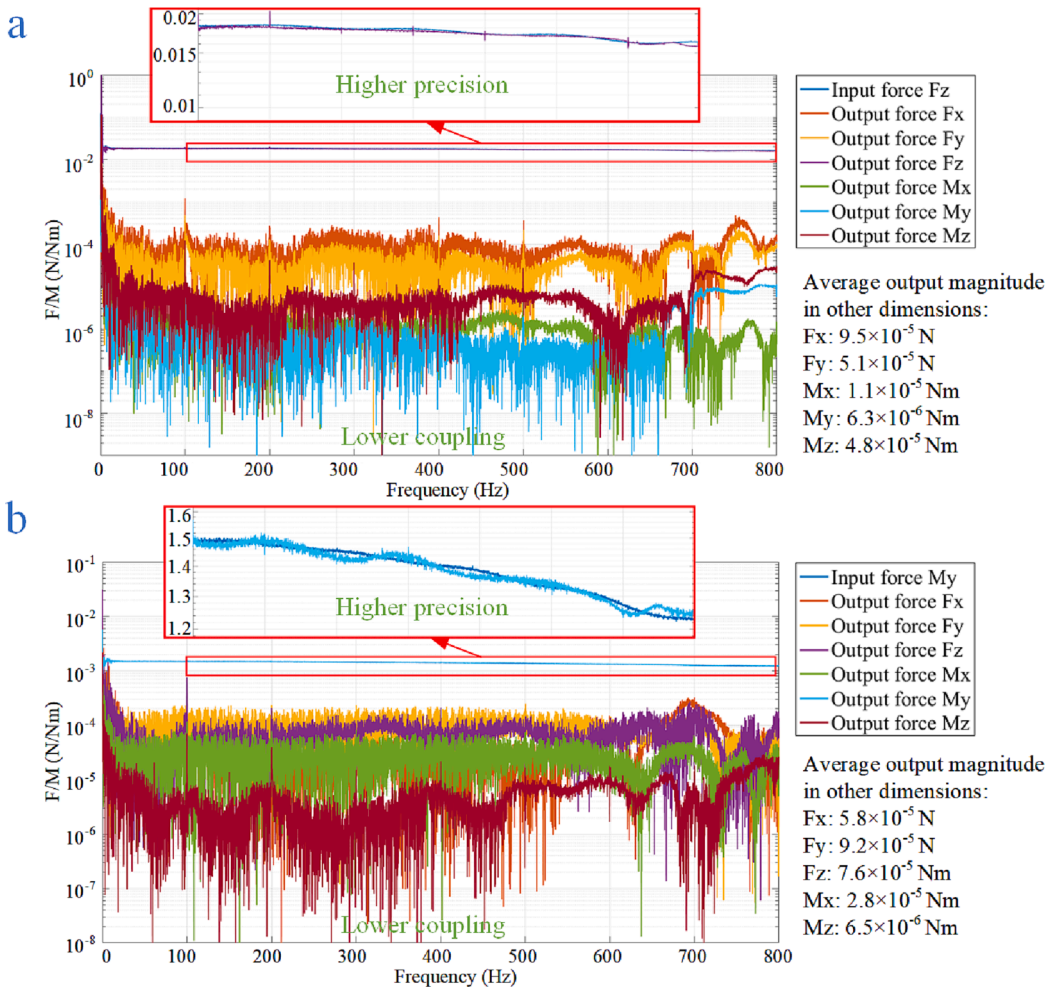

Fig. 14. Comparison of input and output forces based on SVM: (a) F_z; (b) M_y.

Table 6
Average relative error rates and cross-coupling error rates for the platform based on the SVR.

Forces/Moments (N/Nm)	**Average relative error rates** & cross-coupling error rates					
	F_x	F_y	F_z	M_x	M_y	M_z
F_x	**2.563**	0.078	0.541	5.374	4.363	6.348
F_y	0.078	**3.219**	0.284	6.207	6.535	4.376
F_z	0.276	0.031	**3.418**	4.813	5.233	5.876
M_x	0.735	0.167	0.068	**2.264**	1.968	2.758
M_y	0.091	0.026	0.037	0.879	**1.116**	0.546
M_z	0.423	0.611	0.286	1.274	0.465	**1.037**

iterations to 10,000 and the error of stopping training to 10^{-3}. The measured results of the z-axis force and y-axis moment are plotted in Fig. 14, and the statistics of the average relative error rates and cross-coupling error rates are summarized in Table 6. The maximum relative error rate and cross-coupling error rate are 3.42% and 6.54%, respectively.

4. Results and discussion

The comparison of the measurements in Sections 3 and 4 reveals that the SVR based dynamic calibration has less cross-coupling but higher measurement accuracy, which solves the problems arising from traditional dynamic measurements perfectly. Therefore, the novel calibration and measurement methods are more effective and can be used to improve the performance of the load sharing measurement platform. There are, of course, a number of factors that affect the performance of LS based and SVR based measurements, such as the number of calibrations, the accuracy of the input forces, and the choice of kernel function. However, no matter how much we improve the performance of LS based measurements, it still cannot exceed that of SVR based measurements, which further confirms the superiority of the proposed method. Besides, the SVR based dynamic calibration also excels in the important aspect of efficiency.

The above study is based on the proposed load sharing measurement platform. Thus, it is difficult to compare the measurement performance of the novel calibration method applied to the novel measurement platform with that of other articles. Also, no studies have been carried out on non-linear dynamic calibration and measurement.

As for model parameter uncertainty, it has a significant impact on, for example, the measurement principles in the articles [8,9], but the platform presented in this paper is dynamically calibrated so that the parameter uncertainty has a minimal impact on its performance. The exact effect of parameter uncertainty on both methods is an interesting and needed in-depth study, which we will pursue in the future.

The uses of the proposed platform and method are not limited to dynamic force measurements of vibration sources in spacecraft but can also be applied to clinical applications [29], precision instruments, structural optimization of materials [30–32], etc.

5. Conclusion

Lack of load capacity and non-linearity, which influence measurement accuracy, are problems with traditional large dynamic force measuring platforms. This paper mainly shows a load sharing dynamic disturbance force measuring platform aimed at the existing problem. The structural optimization and calibration methods are investigated to improve the platform's performance.

A load-sharing ring and four three-output sensors are distributed in parallel to increase the platform's loading capacity and base frequency. To further improve the characteristics of the platform structurally, the MIGA algorithm is used to optimize the structural parameters of the platform. Compared to the platform optimized by the ASA algorithm, the platform based on MIGA has the advantage of lower manufacturing costs and installation requirements but better load capacity, which demonstrates the superiority of MIGA for structural optimization.

In addition, the novel dynamic calibration method improves the measurement accuracy of the platform by avoiding matrix singularity and taking into account platform non-linearity. The maximum average relative error rate and cross-coupling error rate in the measurement of six-dimensional forces/moments using the conventional LS dynamic calibration method are 9.98% and 15.39%, respectively, while the corresponding error rates based on the SVR method are 3.42% and 6.54%. The results demonstrate that the SVR based technique outperforms the LS in terms of measurement accuracy and decoupling ability.

With joint effort, this article improves the measurement performance of the measuring platform through both structure and calibration method, giving a reference for the design or measurement of measuring devices with similar structure or principles. In the future, we will investigate in depth the performance differences of various non-linear algorithms that can be applied to the dynamic decoupling of vibration sources' disturbance forces.

Funding

This work was supported by the National Natural Science Foundation of China (No. 11972343) and the National Natural Science Foundation of China (No. 62235018).

Declaration of Competing Interest

The authors declare that they have no known competing financial interests or personal relationships that could have appeared to influence the work reported in this paper.

Data availability

The authors do not have permission to share data.

Acknowledgment

We thank Kaiying for her assistance throughout the research process, including care, tolerance, etc.

References

[1] Y. Sun, D.S. Deng, H.B. Yuan, Precision of the Chinese Space Station Telescope (CSST) stellar radial velocities, Res. Astron. Astrophys. 21 (4) (2021) 092, https://doi.org/10.1088/1674-4527/21/4/92.

[2] Y.e. Cao, Y. Gong, Z.-Y. Zheng, C. Xu, Calibrating photometric redshift measurements with the Multi-channel Imager (MCI) of the China Space Station Telescope (CSST), Res. Astron. Astrophys. 22 (2) (2022) 025019.

[3] M.Y. Xia, Z.B. Xu, K. Han, Q. Huo, A. Li, Dynamic disturbance force measurement platform for large moving device in spacecraft, J. Sound Vib. 447 (2019) 61–77, https://doi.org/10.1016/j.jsv.2019.01.053.

[4] L. Li, L. Tan, L. Kong, D. Wang, H. Yang, The influence of flywheel micro vibration on space camera and vibration suppression, Mech. Syst. Sig. Process. 100 (2018) 360–370.

[5] T.K. Jang, B.S. Lim, K.K. Moon, The canonical stewart platform as a six DOF pose sensor for automotive applications, J. Mech. Sci. Technol. 32 (2018) 5553–5561, https://doi.org/10.1007/s12206-018-1101-0.

[6] Y.L. Hou, et al., Optimal design of a hyperstatic Stewart platform-based force/torque sensor with genetic algorithms, Mechatronics 19 (2) (2009) 199–204, https://doi.org/10.1016/j.mechatronics.2008.08. 002.

[7] Z.Y. Jia, S. Lin, W. Liu, Measurement method of six-axis load sharing based on the Stewart platform, Measurement 43 (3) (2010) 329–335, https://doi.org/10.1016/j.measurement.2009.11.005.

[8] Y.-J. Li, B.-Y. Sun, J. Zhang, M. Qian, Z.-Y. Jia, A novel parallel piezoelectric six-axis heavy force/torque sensor, Measurement 42 (5) (2009) 730–736.

[9] Y.J. Li, J. Zhang, Z.Y. Jia, et al., A novel piezoelectric 6-component heavy force/moment sensor for huge heavy-load manipulator's gripper, Mech. Syst. Sig. Process. 23 (5) (2009) 1644–1651, https://doi.org/10.1016/j. ymssp.2009.02.004.

[10] Y.J. Li, J. Zhang, Z.Y. Jia, et al., Research on a novel parallel spoke piezoelectric 6-DOF heavy force/torque sensor, Mech. Syst. Sig. Process. 36 (1) (2013) 152–167, https://doi.org/10.1016/j.ymssp.2012.03.016.Y.J. Li, et al.

[11] Y.J. Li, et al., Research on the parallel load sharing principle of a novel self-decoupled piezoelectric six-dimensional force sensor, ISA Trans. 70 (2017) 447–457, https://doi.org/10.1016/j. isatra.2017.07.008.

[12] S.D. Moosavi Nasab, A. Beiranvand, M. Tale Masouleh, F. Bahrami, A. Kalhor, Design and development of a multi-axis force sensor based on the hall effect with decouple structure, Mechatronics 84 (2022) 102766.

[13] R.A.S.I. Subad, M.M.H. Saikot, K. Park, Soft Multi-Directional Force Sensor for Underwater Robotic Application, Sensors22.10 22 (10) (2022) 3850.

[14] Y. Sun, Y. Liu, T. Zou, M. Jin, H. Liu, Design and optimization of a novel six-axis force/torque sensor for space robot, Measurement 65 (2015) 135–148.

[15] K. Han, L. Chen, M. Xia, Q. Wu, Z. Xu, G. Wang, Design and optimization of a high sensitivity joint torque sensor for robot fingers, Measurement 152 (2020) 107328.

[16] A. Nandy, D. Chakraborty, M.S. Shah, Optimal sensors/actuators placement in smart structure using island model parallel genetic algorithm, Int. J. Comput. Methods 16 (06) (2019) 1840018.

[17] W.-W. Zhang, H. Qi, Z.-Q. Yu, M.-J. He, Y.-T. Ren, Y. Li, Optimization configuration of selective solar absorber using multi-island genetic algorithm, Sol. Energy 224 (2021) 947–955.

[18] Z.P. Wang, J. Ma, L. Zhang, State-of-health estimation for lithium-ion batteries based on the multi-island genetic algorithm and the Gaussian process regression, IEEE Access 5 (2017) 21286–21295, https://doi.org/10.1109/access.2017.2759094.

[19] J. Liu, M. Li, L. Qin, J. Liu, Active design method for the static characteristics of a piezoelectric six-axis force/torque sensor, Sensors 14 (1) (2014) 659–671.

[20] S.A. Liu, H.L. Tzo, A novel six-component force sensor of good measurement isotropy and sensitivities, Sens. Actuators, A 100 (2-3) (2002) 223–230, https://doi.org/10.1016/S0924-4247(02)00135-8.

[21] Q.K. Liang, D. Zhang, Q.J. Song, et al., Design and fabrication of a six-dimensional wrist force/torque sensor based on E-type membranes compared to cross beams, Measurement 43 (10) (2010) 1702–1719, https://doi.org/10.1016/j.measurement. 2010.09.010.

[22] Y.-J. Wang, C.-W. Hsu, C.-Y. Sue, Design and calibration of a dual-frame force and torque sensor, IEEE Sens. J. 20 (20) (2020) 12134–12145.

[23] H.S. Oh, U. Kim, G. Kang, J.K. Seo, H.R. Choi, Multi-axial force/torque sensor calibration method based on deep-learning, IEEE Sens. J. 18 (13) (2018) 5485–5496.

[24] Y.-J. Li, G.-C. Wang, X. Yang, H. Zhang, B.-B. Han, Y.-L. Zhang, Research on static decoupling algorithm for piezoelectric six axis force/torque sensor based on LSSVR fusion algorithm, Mech. Syst. Sig. Process. 110 (2018) 509–520.

[25] X. Wang, Z. Xu, M. Xia, S. He, H. Li, Q. Wu, Research on a six-degree-of-freedom disturbance force and moment simulator for space micro-vibration experiments, J. Sound Vib. 432 (2018) 530–548.

[26] M. Xia, C. Zhou, E. Zhang, C. Han, Z. Xu, A dynamic disturbance force measurement system based on array sensor for large moving device in spacecrafts, J. Sound Vib. 535 (2022) 117069.

[27] C.B. Zhou, M.Y. Xia, Z.B. Xu, Design and optimization of a quadrupedal dynamic disturbance force measurement platform using strain gauges, Mech. Syst. Sig. Process. (2022), 110032, https://doi.org/10.1016/j.ymssp.2022.110032.

[28] C.B. Zhou, M.Y Xia, and Z.B. Xu. A six dimensional dynamic force/moment measurement platform based on matrix sensors designed for large equipment. Sensors and Actuators A: Physical (2022): 114085. https://doi.org/10.1016/j.sna.2022.114085.

[29] F. Orsini, et al., A method for force platforms dynamic performances characterization in clinical applications. 2018 IEEE International Symposium on Medical Measurements and Applications (MeMeA), IEEE, 2018.

[30] Y. Wu, Z. Dong, Y. Chen, B. Wang, L. Wang, X. Dai, J. Zhang, X. Wang, Optimization of Pixel Size and Electrode Structure for Ge: Ga Terahertz Photoconductive Detectors, Sensors 22 (5) (2022) 1916.

[31] J.-J. Tao, J. Jiang, S.-N. Zhao, Y. Zhang, X.-X. Li, X. Fang, P. Wang, W. Hu, Y. H. Lee, H.-L. Lu, D.-W. Zhang, Fabrication of 1D Te/2D ReS2 mixed-dimensional van der waals pn heterojunction for high-performance phototransistor, ACS Nano 15 (2) (2021) 3241–3250.

[32] J.-J. Tao, H.-P. Ma, K.-P. Yuan, Y. Gu, J.-W. Lian, X.-X. Li, W. Huang, M. Nolan, H.-L. Lu, D.-W. Zhang, Modification of 1D TiO 2 nanowires with GaO x N y by atomic layer deposition for TiO 2@ GaO x N y core–shell nanowires with enhanced photoelectrochemical performance, Nanoscale 12 (13) (2020) 7159–7173.